RSC Advances

PAPER

View Article Online
View Journal | View Issue

Cite this: *RSC Adv.*, 2020, **10**, 10285

Activity of $La_{0.75}Sr_{0.25}Cr_{0.5}Mn_{0.5}O_{3-\delta}$, Ni_3Sn_2 and Gd-doped CeO_2 towards the reverse water-gas shift reaction and carburisation for a high-temperature H_2O/CO_2 co-electrolysis†

Nicky Bogolowski, Beatriz Sánchez Batalla, Baekkyoung Shin and Jean-Francois Drillet *

The syngas mixture of CO and H_2, *e.g.* from natural gas reforming, is currently an important feedstock supplier for the synthesis of numerous chemicals. In order to minimize fossil source dependency and reduce global warming, alternative processes to produce syngas, such as high-temperature co-electrolysis of H_2O and CO_2 *via* the internal reverse water-gas shift (RWGS) reaction, may be meaningful. In this study, the influence of the H_2 : CO_2 ratio on the activity, selectivity and stability of the as-prepared $La_{0.75}Sr_{0.25}Cr_{0.5}Mn_{0.5}O_{3-\delta}$ (LSCrM) and Ni_3Sn_2 as well as commercial Ni and Gd-doped CeO_2 (GDC_{20}) powder materials for the reverse RWGS reaction was investigated in a tubular quartz glass reactor at 700 °C and 800 °C and ambient pressure. The highest conversion factor close to the maximum value of 50% for CO was yielded for the LSCrM, Ni and GDC_{20} samples by applying a 0.5 : 0.5 H_2 : CO_2 feed ratio at 800 °C. Similar activity was calculated for the Ni_3Sn_2 alloy after normalization to the Ni mass content. Moreover, all the investigated catalysts exhibited higher selectivity for CO and H_2O products than Ni, with which CH_4 molar concentrations up to 0.9% and 2.4% were collected at 800 °C and 700 °C, respectively. The influence of feed pressure on the carburisation process was inspected in a tubular Ni–Cr reactor. Under a carbon-rich gas mixture at 3 bar and 700 °C, large amounts of graphitic carbon were deposited solely on the Ni sample after 100 h of exposure time. After the exposure of the powder materials to 0.5 : 0.5 and 0.9 : 0.1 H_2 : CO_2 atmospheres for 300 h at 700 °C and 10 bar, traces of amorphous carbon were surprisingly detected only on Ni_3Sn_2 powder *via* Raman microscopy. Thus, because GDC_{20} ist not active for electrochemical H_2 production, LSCrM or a mixture of both LSCrM and GDC_{20} materials appears to be the most promising candidate for Ni substitution in high-temperature H_2O/CO_2 co-electrolysis.

Received 13th January 2020
Accepted 18th February 2020

DOI: 10.1039/d0ra00362j

rsc.li/rsc-advances

1. Introduction

1.1 High temperature H_2O/CO_2 co-electrolysis

Because renewable energy sources are subject to seasonal fluctuations and fossil resources are limited, innovative energy storage strategies are urgently needed.[1,2] High temperature H_2O/CO_2 co-electrolysis is one of the most energetically efficient processes to recycle climate-wrecking CO_2 with green electricity into chemically valuable syngas (a mixture of H_2 and CO), particularly if process vapour is available. This syngas can be further transformed into more valuable products, such as methane, alcohol, hydrocarbons (*e.g.* e-fuels *via* the Fischer–Tropsch process) and chemicals.

Ni cermet is currently the most common cathode material for H_2O/CO_2 co-electrolysis due to its appropriate catalytic activity, high electronic conductivity, low cost and thermal expansion coefficient, which is close to that of the YSZ electrolyte.[3] When using Ni/yttria-stabilized zirconia (YSZ) as a cathode material, it was suggested that CO_2 to CO conversion occurs mainly through the RWGS reaction and to a lesser extent *via* electrochemical CO_2 reduction.[4–6]

However, Ni is subject to degradation due to a variety of mechanisms. Particle agglomeration, densification and migration from the electrolyte/electrode interface are the most important issues responsible for cell degradation, especially at high current density.[7] In addition, Ni is prone to oxidation, which necessitates the addition of reducing gas such as H_2; it also has poor tolerance to impurities[8,9] and favours carburization in a low-humidity hydrocarbon atmosphere. The nature and location of deposited carbon during SOFC operation with a hydrocarbon gas mixture at Ni/YSZ depends on the C–H–O

DECHEMA-Forschungsinstitut, Theodor-Heuss-Allee 25, 60486 Frankfurt a. M., Germany. E-mail: jean.drillet@dechema.de

† Electronic supplementary information (ESI) available. See DOI: 10.1039/d0ra00362j

ratio and operation temperature.[10] A further degradation mechanism at Ni alloys at high temperatures is related to carbon formation, *e.g.* metal dusting *via* carbide formation.[11] At high cell current densities under transport-limiting conditions, carbon monoxide may be reduced to carbon (1).[12] Ni also catalyses the disproportionation of CO (Boudouard reaction) (2), and at high temperature, methane carburisation (3) may occur:[13]

$$CO(g) + H_2(g) \rightarrow C(s) + H_2O(g), \text{ reverse water-gas reaction} \quad (1)$$

$$2CO(g) \rightarrow CO_2(g) + C(s)\ CO, \text{ disproportionation} \quad (2)$$

$$CH_4(g) \rightarrow C(s) + 2H_2(g), \text{ methane carburisation} \quad (3)$$

However, under typical SOEC operating conditions, CO_2 and/or H_2O are present in the reaction gas; therefore, reaction (1) is usually not critical. If the SOEC is operated at higher pressure and lower temperature, the Boudouard reaction (2) and the reduction of CO (3) will be promoted. In previous study, we successfully tested Ni_3Sn_2 as an anode material in direct methane solid oxide fuel cells (DMSOFC), which are usually very favourable for coking reactions.[14] Interestingly, this material exhibited excellent stability against carbon formation over more than 650 h at 850 °C; this was explained by the occupation of carbon nucleation sites by Sn atoms in the vicinity of Ni atoms.[15] Therefore, the intermetallic Ni_3Sn_2 phase was considered as a possible cathode material for co-electrolysis.

Because of their high redox stability, relatively good mixed ionic and electronic conductivity and low activity for carbon formation, perovskite oxides such as (La,Sr)(Cr,Mn)O_3, (La,Sr)TiO_3, Sr(Fe,Mo)O_3, (La,Sr)VO_3 and (La,Sr)FeO_3 have been investigated as possible substitution materials for nickel in H_2O/CO_2 co-electrolysis cathodes.[3] Maiti *et al.* investigated oxygen vacancies and surface terminations along the (100) and (110) planes for $La_{1-x}Sr_xFe_{1-y}Co_yO_{3-\delta}$ by density functional theory (DFT). The carbon dioxide adsorption strength, a key descriptor for CO_2 conversion reaction, was found to increase on oxygen-vacant surfaces. Amongst all the surface terminations, the lanthanum–oxygen terminated surface exhibited the strongest CO_2 adsorption strength.[16]

One of the most studied materials is the p-type semiconductor (La, Sr)(Cr, Mn)O_3, depicted in this work as LSCrM, with electronic conductivity > 1 S cm^{-1} in reducing atmosphere. However, its relatively low ionic conductivity can be enhanced by adding *e.g.* CeO_2 or ZrO_2.[3] Yoon *et al.*[17] reported an impressive increase of cell performance under steam/CO_2 co-electrolysis after CeO_2 and Pd addition. A LSCrM with a highly dispersed GDC nanoparticle cathode was tested by Yue *et al.*[18] for CO_2 electrolysis. They mentioned a reduction in cell polarization resistance R_p, associated with improvement of the electrochemical and catalytic activity from the nanostructured GDC phase. By doping the GDC co-impregnated LSCrM material with Pd, the cathodic activity was comparable with that of the Ni/YSZ state-of-the-art catalyst, and the stability was enhanced. The activity of YbScSZ electrolyte-supported SOEC with symmetrical LSCrM electrodes was evaluated by Torrell *et al.*[19] They demonstrated that LSCrM was a suitable cathode material for H_2O/CO_2 co-electrolysis, even without addition of reducing gas such as H_2.

1.2 RWGS reaction

While the water-gas shift reaction (WGS) takes place at temperatures below 720 °C, the reversible water-gas shift reaction (RWGS) is endothermic and occurs at temperatures above 720 °C. Depending on the catalyst used, syngas can be produced by (i) electrochemical reduction of both H_2O and CO_2 at a heterogeneous catalyst, *e.g.* nickel, or *via* (ii) electrochemical H_2O reduction to hydrogen followed by a homogeneous/heterogeneous RWGS reaction, as follows:

$$H_2(g) + CO_2(g) \leftrightarrows CO(g) + H_2O(g) \quad (4)$$

The reaction steps of the homogeneous RWGS reaction are described by the single gas-phase chain-reaction in Bradford's model, where M refers to any gas-phase molecule:[20]

$$H_2 + M \rightarrow 2H + M, \text{ dissociation of hydrogen} \quad (5)$$

$$H + CO_2 \leftrightarrows CO + OH, \text{ reaction between H and } CO_2 \quad (6)$$

$$OH + H_2 \leftrightarrows H_2O + H, \text{ reaction between OH and } H_2 \quad (7)$$

$$M + 2H \rightarrow M + H_2, \text{ reassociation of hydrogen} \quad (8)$$

The mechanism of the heterogeneous RWGS reaction still remains unclear; meanwhile, two main interpretations prevail. Pekridis *et al.*[21] suggested that at Pt, CO production occurs *via* formation of formate adsorbate on the catalyst surface according to reactions (9–15). This mechanism was also supported by FT-IR spectra published by Sun *et al.*,[22] who investigated RWGS at a $CuO/ZnO/Al_2O_3$ catalyst; they claimed to observe the formation of mono (C_{ads}) and bidentate (C_{ads} and O_{ads}) formate species and their further decomposition to CO.

$$CO_2 + * \leftrightarrows CO_2^*, \text{ molecular adsorption of } CO_2 \quad (9)$$

$$H_2 + 2* \leftrightarrows 2H*, \text{ dissociative adsorption of } H_2 \quad (10)$$

$$H* + CO_2^* \leftrightarrows COOH* + *, \text{ formate formation} \quad (11)$$

$$COOH* + * \leftrightarrows CO* + OH*, \text{ formation of CO and hydroxyl} \quad (12)$$

$$OH* + H* \leftrightarrows H_2O* + *, \text{ water formation} \quad (13)$$

$$H_2O* \leftrightarrows H_2O + *, \text{ water desorption} \quad (14)$$

$$CO* \leftrightarrows CO + * \text{ CO, desorption} \quad (15)$$

where * is a vacant site.

Fujita *et al.*[23] investigated the RWGS reaction products at Cu/ZnO by FTIR and found that the reaction pathway proceeds first through oxidation of the catalyst surface by oxygen species from CO_2 dissociation and second by reduction of Cu(I) to metallic Cu in the presence of H_2. The formation of the formate

Table 1 Composition, crystalline structure, particle size and BET surface area of pristine LSCrM, Ni_3Sn_2, GDC_{20} and Ni

Catalyst	Composition	Crystalline structure[c]	Particle size[d] (μm)	BET ($m^2\ g^{-1}$)
LSCrM	$La_{0.76}Sr_{0.24}Cr_{0.57}Mn_{0.43}O_3$[a] $La_{0.79}Sr_{0.21}Cr_{0.58}Mn_{0.42}O_3$[b]	Trigonal perovskite	0.5–1	2.4
Ni_3Sn_2	Ni_3Sn_2[b]	Orthorhombic	10–15	0.6
GDC_{20}	$Gd_{0.23}Ce_{0.77}O_2$[b]	Cubic	0.15–0.55	15.3
Ni	Ni	Cubic	2–6	0.4

[a] From ICP-MS. [b] From EDX (see Fig. 5). [c] From XRD (see Fig. 3). [d] From SEM (see Fig. 4).

intermediate described by (11) and (12) is replaced by that of CO, O and OH adsorbates according to the following mechanism:

$$CO_2^* + * \leftrightarrows CO* + O*, \text{ dissociative adsorption of } CO_2 \quad (16)$$

$$O* + H* \leftrightarrows OH*, \text{ formation of adsorbed hydroxyl} \quad (17)$$

Studies on heterogeneous RWGS focus principally on Pt-[24] Cu-[25] and Ni-based[26] catalysts. In another study, conversion of CO_2 to CO close to thermodynamic limit was yielded at Pd, Cu and Ni catalysts supported on Al_2O_3.[27] Wolf *et al.* studied the RWGS reaction kinetics at Ni/Al_2O_3 in a fixed-bed reactor and found that a CO_2 equilibrium conversion of almost 80% at 900 °C was achieved within a residence time of less than 100 ms.[28]

Another interesting candidate is CeO_2 because of its well-tuneable ionic and electronic conductivity, especially at high temperature and low oxygen partial pressure.[29] Interestingly, addition of certain doping materials, such as gadolinium, may increase both conductivities. An electronic conductivity of 0.2 S cm^{-1} in air and an electronic conductivity of 1.44 S cm^{-1} in $p_{O_2} = 10^{-15}$ bar are reported for $Ce_{0.8}Gd_{0.2}O_{1.9}$ in;[30] thus, it is a suitable cathode, anode and electrolyte material in solid oxide fuel cells (SOFCs). Wang *et al.*[26] developed a Ni/CeO_2 catalyst with high activity, selectivity and stability for the RWGS reaction. Liu *et al.* showed a stable increase in CO_2 conversion over a Ni/CeO_2 catalyst prepared by a polymer-assisted co-precipitation method.[31] Furthermore, Kovacevic *et al.* studied the influence of the morphology of the CeO_2 catalyst on the catalytic activity for the RWGS reaction. They showed that CeO_2 cubes were the most active and claimed that the (100) crystal plane in this CeO_2 cubes have higher reactivity due to the lower coordination numbers in these facets. Thus, cube catalysts are more active for the RWGS than nanoparticle and rod geometries, which are enclosed by almost inert (111) crystal planes.[32]

In this work, the activities of $La_{0.75}Sr_{0.25}Cr_{0.5}Mn_{0.5}O_{3-\delta}$ perovskite, Ni_3Sn_2 alloy and GDC_{20} for the RWGS reaction were investigated in a quartz tube reactor at 700 °C and 800 °C in different H_2 : CO_2 atmospheres for the first time and compared to that of Ni. The testing of GDC_{20} was motivated by the fact that gadolinium-doped CeO_2 (GDC_{20}) is normally used as an interlayer between the electrolyte and electrode in SOEC to avoid $SrZrO_3$ formation and increase oxygen mobility and because CeO_2 is active for the WGS reaction. Additionally, the coking behaviour of LSCrM, Ni_3Sn_2, GDC_{20} and Ni was evaluated in a NiCr tubular reactor at 700 °C up to 10 bar in different H_2 : CO_2 atmospheres.

2. Results

2.1 Physicochemical characterisation of the pristine LSCrM, Ni_3Sn_2, GDC_{20} and Ni samples

The most relevant data about the composition of the powder materials (EDX), crystalline structures (XRD), particle sizes (SEM) and BET surface areas of the catalysts are summarized in

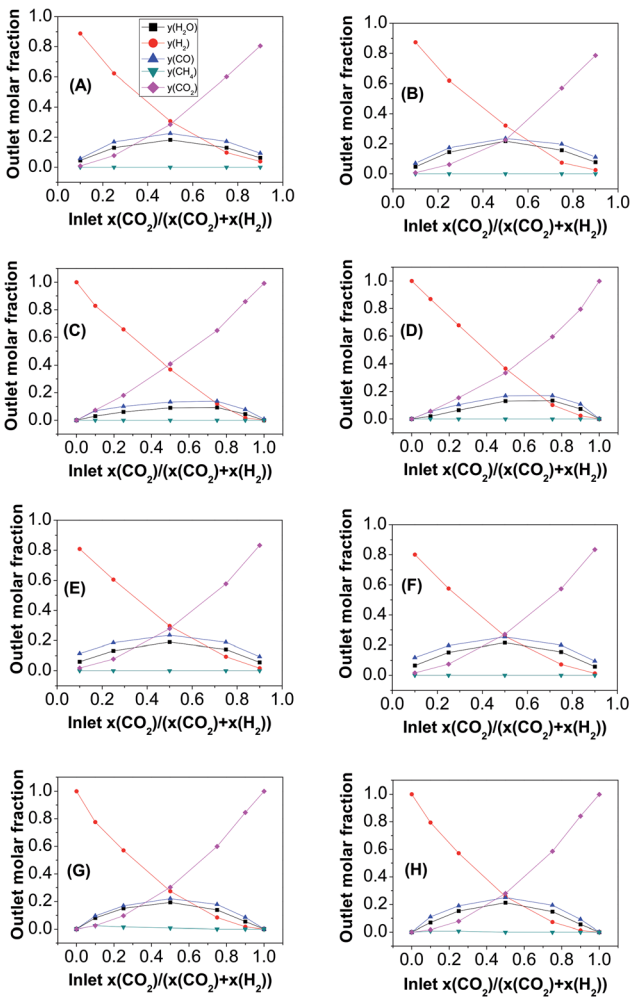

Fig. 1 Influence of the H_2 : CO_2 molar inlet composition on the RWGS reaction product concentration with (A and B) LSCrM, (C and D) Ni_3Sn_2, (E and F) GDC_{20} (G and H) Ni.

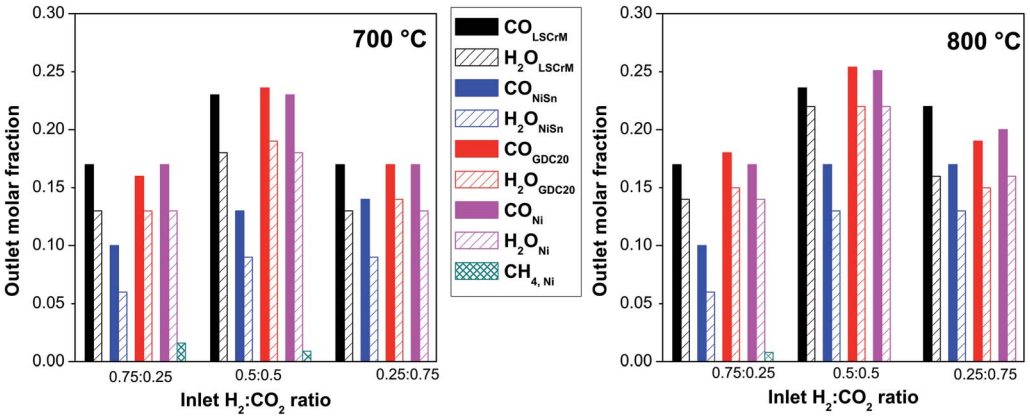

Fig. 2 Summaries of the H_2O, CO and CH_4 reaction product molar fractions at the reactor outlet as a function of the 2 temperatures of 700 °C (left) and 800 °C (right) and 3 relevant H_2 : CO_2 educt molar fractions at the reactor inlet.

Table 1. Extensive comments on the EDX, SEM and XRD analysis are provided later in the text, where the influence of the experimental parameters on the material properties is discussed in more detail. The catalyst composition of LSCrM was also measured by inductively coupled plasma mass spectrometry (ICP-MS). Except for slight deviations in the stoichiometric factors of La and Sr, a similar composition was measured.

2.2 Tests in a tubular quartz glass reactor at 1 bar

2.2.1 Blind experiments. First, blind experiments without any catalyst powder in the Al_2O_3 crucible were performed in both tube reactors. By using a 0.5 : 0.5 equimolar H_2 : CO_2 feed, CO molar fractions of 0.016 and 0.035 and CO_2 conversion factors

$$\frac{[CO]_{out}}{[CO_2]_{in}} \times 100 \quad (18)$$

of 3.2% and 7.0% were measured by gas chromatography at the quartz glass tube reactor outlet at 700 °C and 800 °C, respectively (see Fig. S1 in the ESI†). In contrast, CO molar fractions of 0.044 and 0.101 (conversion factors of 8.8% and 20.2%) were detected at the Ni–Cr reactor outlet at 10 bar for 700 °C and 800 °C, respectively (see Fig. S2 in the ESI†). Due to its nickel-

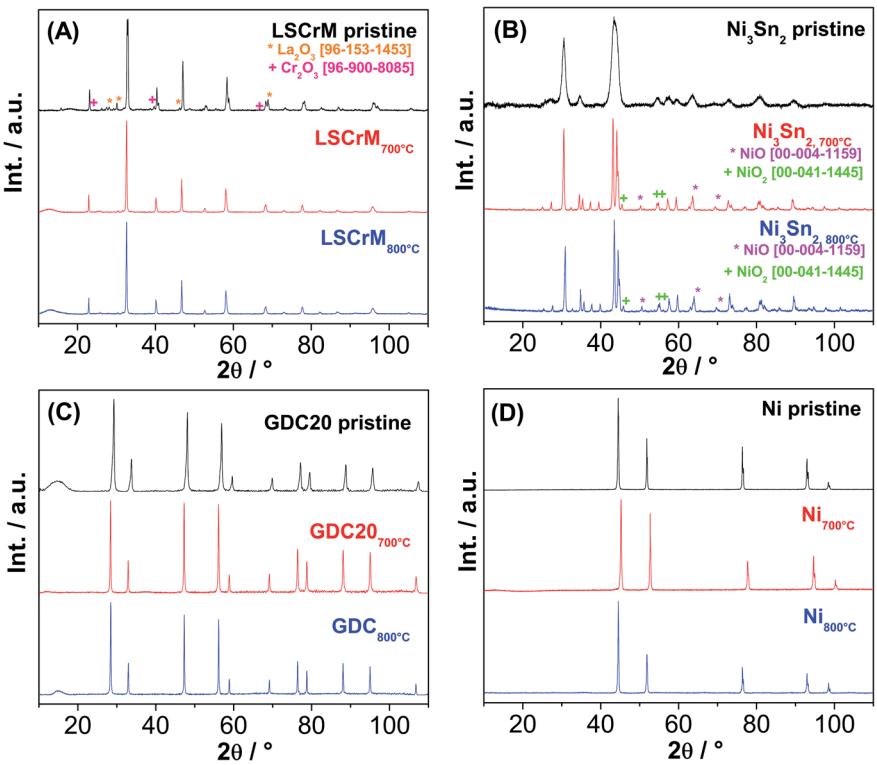

Fig. 3 XRD patterns of (A) LSCrM, (B) Ni_3Sn_2, (C) GDC_{20} and (D) Ni before and after catalytic activity tests at 700 °C and 800 °C.

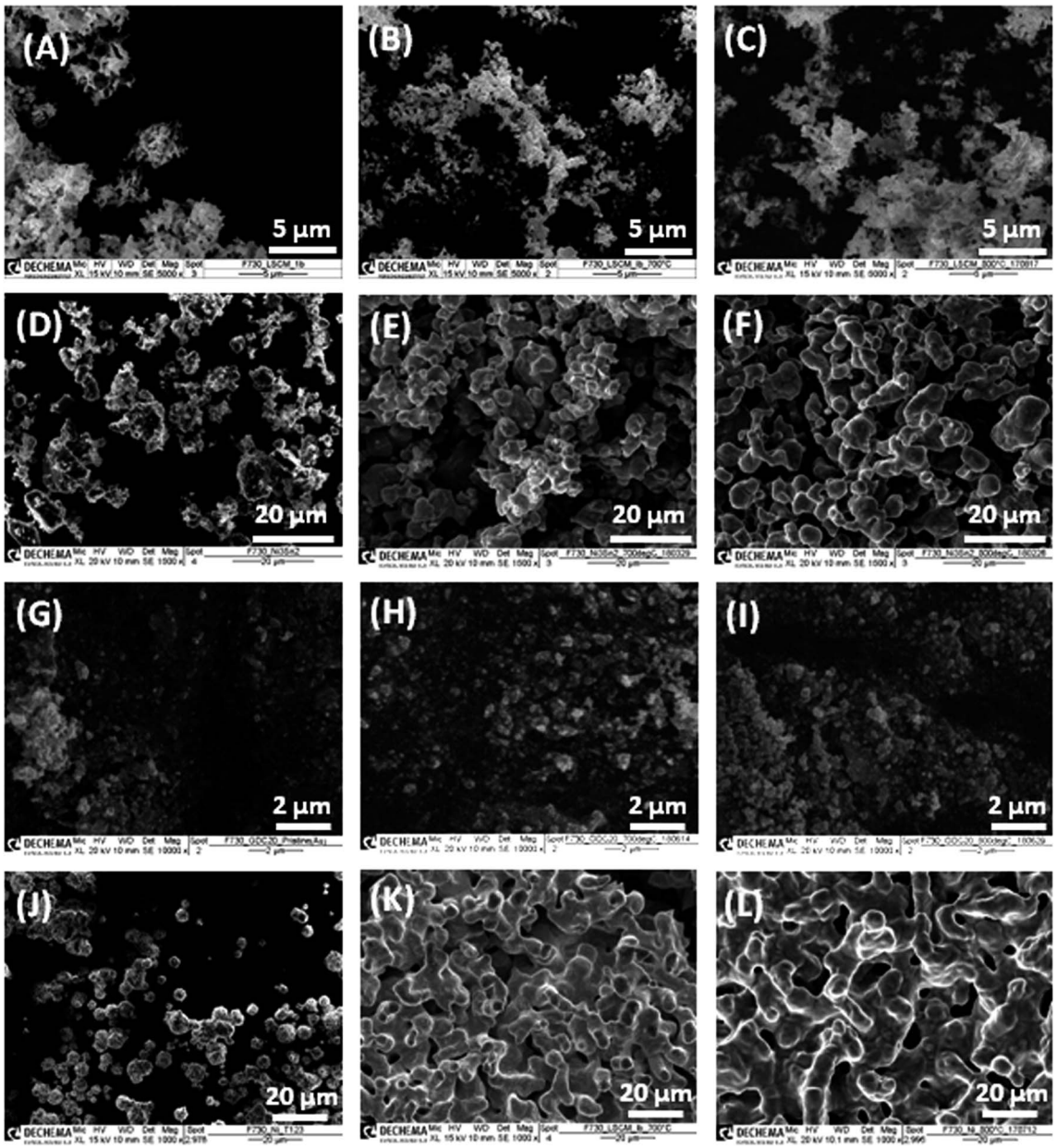

Fig. 4 SEM micrographs of (A–C) LSCrM, (D–F) Ni_3Sn_2, (G–I) GDC_{20} and (J–L) Ni (left) before and after catalytic activity tests performed at (middle) 700 °C and (right) 800 °C.

rich (46% Ni, 34.7% Cr, …) metallic composition, this material is unsuitable for catalytic experiments. These results are in good accordance with those reported by Bustamente *et al.*, who calculated CO_2 conversion factors of about 0.1% and up to 40% with and without Ni, respectively, in an Inconell® 600 quartz glass reactor at 900 °C.[20]

2.2.2 Evaluation of the catalytic activity of powder materials for the RWGS reaction. The catalytic activities of LSCrM, Ni_3Sn_2, GDC_{20} and Ni for the RWGS reaction as a function of temperature (700 °C and 800 °C) and of different selected inlet $H_2 : CO_2$ gas compositions of $0 \leq x(CO_2) \leq 1$ for the Ni-based catalysts and $0.1 \leq x(CO_2) \leq 0.9$ for LSCrM and GDC_{20} to prevent complete reduction are presented in Fig. 1.

Because the RWGS is an endothermic reaction, the molar fractions of the CO and H_2O reaction products at 800 °C were, as expected, slightly higher than those measured at 700 °C. The

Table 2 Compositions of the catalysts before and after the catalytic activity tests at 700 °C and 800 °C calculated from the EDX spectra with an integration error of ±0.01

Catalyst	LSCrM	Ni_3Sn_2	GDC_{20}
Pristine	$La_{0.79}Sr_{0.21}Cr_{0.58}Mn_{0.42}O_{3-\delta}$	$Ni_{2.96}Sn_{2.04}$	$Gd_{0.23}Ce_{0.77}O_{2-\delta}$
@700 °C	$La_{0.76}Sr_{0.24}Cr_{0.62}Mn_{0.38}O_{3-\delta}$	$Ni_{3.35}Sn_{1.65}$	$Gd_{0.23}Ce_{0.77}O_{2-\delta}$
@800 °C	$La_{0.71}Sr_{0.29}Cr_{0.63}Mn_{0.37}O_{3-\delta}$	$Ni_{2.93}Sn_{2.07}$	$Gd_{0.23}Ce_{0.77}O_{2-\delta}$

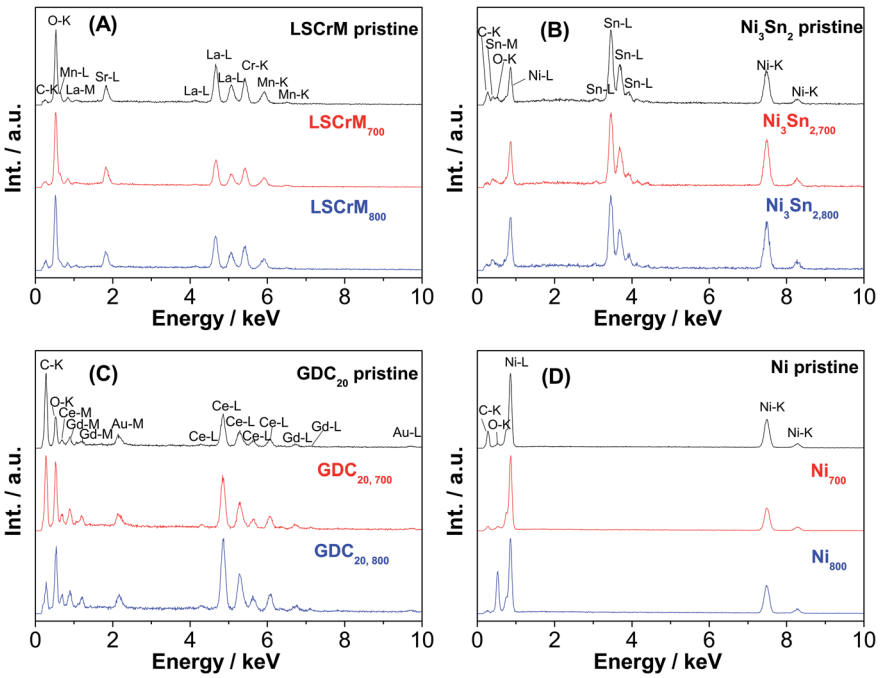

Fig. 5 EDX spectra of (A) LSCrM, (B) Ni_3Sn_2, (C) GDC_{20} and (D) Ni before and after catalytic activity tests at 700 °C and 800 °C.

highest conversion factor was yielded with a 0.5 : 0.5 H_2 : CO_2 inlet ratio at the LSCrM, Ni and GDC_{20} samples at both temperatures. It is worth considering that the active Ni mass in Ni_3Sn_2 amounted to 1.7 g (42.6% of the total alloy mass), which correlates well with about half the conversion factor of that yielded at the pure nickel material. It appears that a combination of low temperature (here, 700 °C) and high hydrogen concentration favours CH_4 production, especially at the nickel material. At H_2 : CO_2 = 0.9 : 0.1 and 0.75 : 0.1 inlet gas feeds, 2.4% and 1.6% CH_4 were detected at 700 °C and 0.9% and 0.8% CH_4 were detected at 800 °C, respectively. Even at a H_2 : CO_2 molar ratio of 0.5 : 0.5 at 700 °C, 0.8% CH_4 was formed. At the Ni_3Sn_2, LSCrM and GDC_{20} samples, no methane was detected.

For better clarity and easier interpretation, the activity results of only three relevant gas compositions were converted into a bar graph, as displayed in Fig. 2. At 800 °C and with a 0.5 : 0.5 H_2 : CO_2 gas mixture, CO concentrations of 25.4% at GDC_{20}, 23.6% at LSCrM and 25.1% at Ni were detected by GC. For these measurements, an absolute margin of error of ±1% was estimated.

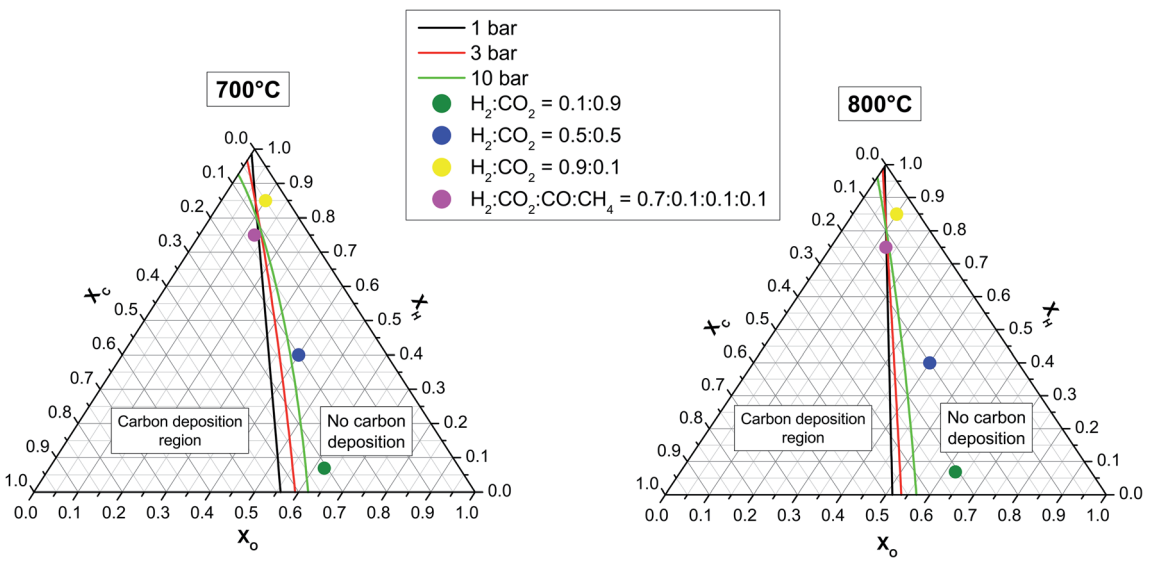

Fig. 6 C–H–O ternary phase diagrams at 700 °C (left) and 800 °C (right) with delimiting boundary lines for the formation of graphitic carbon at three different pressures. The four dots reflect the C–H–O compositions of the 3 different H_2 : CO_2 and carbon-rich mixtures.

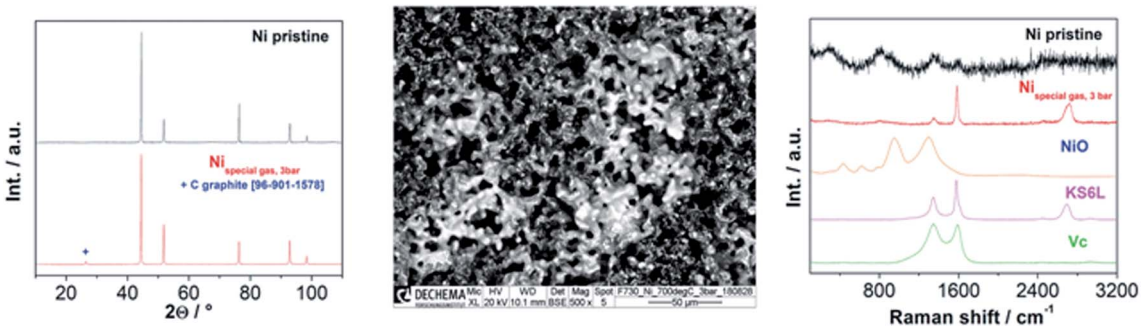

Fig. 7 XRD pattern (left), BSE micrograph (middle) and Raman spectrum (right) of Ni after the long-term stability test in a carbon-rich atmosphere at 700 °C and 3 bar. For comparison, the Raman spectra of amorphous carbon Vulcan X72R (Vc), graphitic carbon KS6L and NiO are added.

Because the kinetics of a heterogeneous reaction is much faster than that of a homogeneous reaction, we assume that in our work, the influence of the values obtained from the blind experiment in the quartz glass reactor without catalyst can be neglected. When we compared the maximum theoretical water molar fraction of 24.5% calculated by FactSage with the measured fractions (21.7%, 21.6% and 21.3% for LSCrM, GDC_{20} and Ni, respectively, in $H_2 : CO_2 = 0.5 : 0.5$ @ 800 °C), the margin of error of the water measurement delivered by the humidity sensor is assumed to be in the range of 1–3%.

Interestingly, GDC_{20} and LSCrM are more selective for the RWGS reaction than Ni because no CH_4 was detected at the reactor outlet. The excellent conversion factor of GDC_{20} for the RWGS reaction can also be ascribed to its 38 times higher BET surface area compared to that of nickel. Because the CO_2 conversion factors at 800 °C for the 0.5 : 0.5 $CO_2 : H_2$ mixture are in the range of 48–50% for all materials, with the exception of Ni alloy, and are almost the same as the calculated thermodynamic equilibrium value of 49%, it can be concluded that our reactor design allowed very good convection and diffusion of educts and products into and out of the Al_2O_3 crucible as well as excellent catalyst accessibility. By using a fixed-bed quartz tube reactor with an 8 mm inner diameter, Liu *et al.*[31] reported a conversion factor of about 40% for a Ni/CeO_2 catalyst in $H_2 : CO_2 = 0.5 : 0.5$ and a gas-flow of 100 ml min^{-1}, but at 600 °C and at a much higher space velocity of 120.000 h^{-1}. At a $H_2 : CO_2$ ratio of 0.8 : 0.2 and with a normalized hourly space velocity of 30 000 ml g^{-1} h^{-1}, with an overall gas flow of 100 ml min^{-1} and assuming an ideal gas, a CO formation rate of 378.9 μmol min^{-1} g^{-1} can be calculated for a conversion factor of 50%. At 700 °C, a conversion factor of about 44% and a CO formation rate of 245.4 μmol min^{-1} g^{-1} were calculated, which may be related to the slower kinetics at this temperature. This is comparable to the CO formation rate of 300 μmol min^{-1} g^{-1} measured by Daza *et al.*[33] for $La_{0.75}Sr_{0.25}CoO_{3-\delta}$ at 850 °C with previously reduced 10% H_2/He at 600 °C for 30 min (total flow rate 50 sccm). The best results in terms of mass activity and selectivity for the RWGS reaction were yielded at the LSCrM and GDC_{20} catalysts.

2.2.3 XRD characterization after testing. Fig. 3 compares the X-ray diffractograms of the LSCrM, Ni_3Sn_2, GDC_{20} and Ni powder samples before and after the catalytic tests, including the cooling procedure in reductive atmosphere. While the XRD patterns of GDC_{20} and Ni underwent no notable change, LSCrM and Ni_3Sn_2 were subjected to phase purification and segregation, respectively. Interestingly, the small additional peaks associated with La_2O_3 and Cr_2O_3 phases observed in the pristine LSCrM spectra disappeared after the activity tests at 700 °C and 800 °C in the tubular glass reactor, whereas small peaks corresponding to NiO and SnO_2 phase emerged in the Ni_3Sn_2 diffractograms.

2.2.4 SEM/EDX characterization after testing. The morphologies and compositions of the different catalysts after testing were investigated by SEM/EDX and compared with those of the pristine materials. No impurities were detected by EDX in any of the samples. Also, for the LSCrM and GDC_{20} samples, no substantial changes in particle morphology or composition after testing can be observed in the SEM images (Fig. 4 and 5) or in the EDX calculations (Table 2). Even after the 800 °C procedure, both average particle sizes stayed in the same ranges of 0.5–2 μm and 0.15–0.55 μm, respectively.

Additional Au-L and Au-M peaks in the EDX spectrum of the GDC_{20} sample were induced by a gold sputtering step that was carried out in order to improve the poor electronic conductivity of the oxide material. The C-K signal is assigned to the carbon conductive adhesive tape. In contrast, strong sintering of Ni particles from 2 to 6 μm up to 2 to 30 μm is obvious, especially after the test at 800 °C. The driving force of the sintering step is

Table 3 Compositions of the catalysts before and after exposure tests at 3 and 10 bar, calculated from the EDX spectra with an integration error of ±0.01[a]

Composition	LSCrM	Ni_3Sn_2	GDC_{20}
Pristine	$La_{0.79}Sr_{0.21}Cr_{0.58}Mn_{0.42}O_3$	$Ni_{2.96}Sn_{2.04}$	$Gd_{0.23}Ce_{0.77}O_2$
3 bar	$La_{0.81}Sr_{0.19}Cr_{0.66}Mn_{0.34}O_3$	$Ni_{3.34}Sn_{1.67}$	$Gd_{0.21}Ce_{0.79}O_2$
10 bar, (i)	$La_{0.83}Sr_{0.17}Cr_{0.66}Mn_{0.34}O_3$	$Ni_{3.28}Sn_{1.72}$	$Gd_{0.26}Ce_{0.74}O_2$
10 bar, (ii)	$La_{0.80}Sr_{0.20}Cr_{0.67}Mn_{0.33}O_3$	$Ni_{3.16}Sn_{1.84}$	$Gd_{0.21}Ce_{0.79}O_2$
10 bar, (iii)	$La_{0.68}Sr_{0.32}Cr_{0.55}Mn_{0.45}O_3$	$Ni_{3.18}Sn_{1.82}$	$Gd_{0.22}Ce_{0.78}O_2$

[a] 3 bar: Exposure test at 3 bar/700 °C under $H_2 : CO : CH_4 : CO_2 = 0.7 : 0.1 : 0.1 : 0.1$; (i): exposure test at 10 bar/800 °C under $H_2 : CO_2 = 0.9 : 0.1$; (ii): exposure test at 10 bar/700 °C under $H_2 : CO_2 = 0.5 : 0.5$; (iii): exposure test at 10 bar/700 °C under $H_2 : CO_2 = 0.1 : 0.9$.

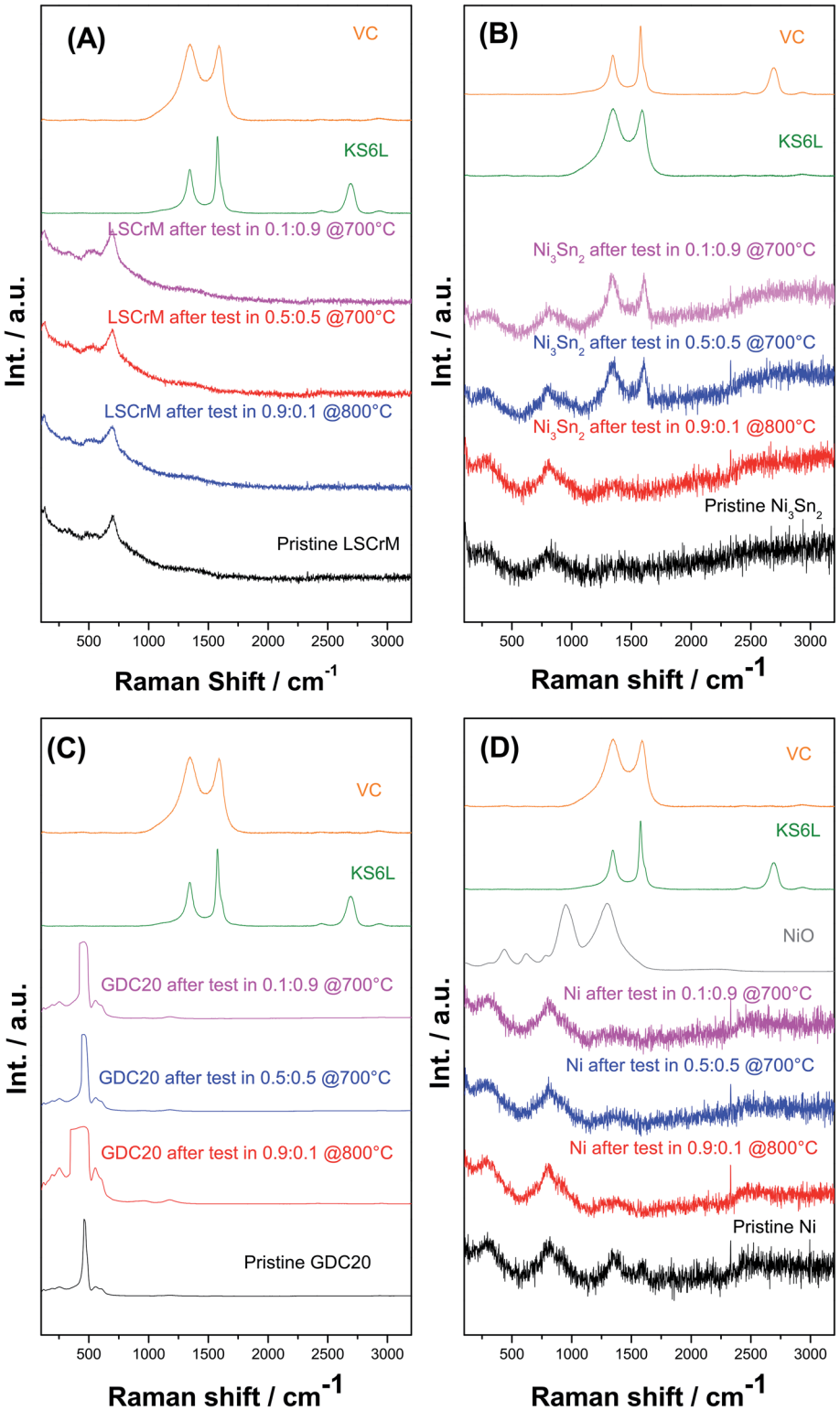

Fig. 8 Raman spectra of (A) LSCrM, (B) Ni_3Sn_2, (C) GDC_{20} and (D) Ni after exposure tests in H_2 : CO_2 atmospheres of 0.1 : 0.9 @ 700 °C (purple), 0.5 : 0.5 @ 700 °C (blue) and 0.9 : 0.1 @ 800 °C (red) at 10 bar pressure and the pristine samples (black). The spectra of graphitic carbon KS6L and amorphous carbon Vulcan XC72R (Vc) are plotted as references for the carbon signals, and the spectra of NiO are plotted as references for the oxidation of Ni and Ni_3Sn_2.

the reduction of the surface/interface energy of the small particles by merging them together in order to form larger particles *via* a mass transport/diffusion process. The sintering activity depends on the melting point and particle size/shape as well. Under SOFC/SOEC conditions, the sintering and densification effects of the nickel particles are attenuated by the

addition of yttrium-stabilized zirconia (YSZ) material as an ionic conductor.[34] With an average particle size in the range of 10–15 μm, the Ni_3Sn_2 particles appear to be less prone to sintering than pure Ni powder. From the pure sintering aspect, LSCrM and GDC_{20} are the best materials.

No substantial change in the EDX spectra after the catalytic activity tests was observed (see Fig. 5). The compositions of the different catalysts calculated from the EDX spectra (see Table 2) slightly differs from the stoichiometric values but lies to some extent within the error margin of the equipment.

2.3 Influence of atmosphere composition, temperature and pressure on carbon formation at the powder materials

2.3.1 Numerical prediction of C–H–O equilibrium at different temperatures and pressures. To evaluate the probability of carbon deposition, calculations were performed with the Phase Diagram and Equilib module in FactSage thermochemical software (version 6.1). Phase diagram calculations in FactSage are based on a thermodynamically consistent theory of generalized phase diagram mapping. The Equilib module minimizes the Gibbs energy and calculates the concentrations of chemical species when specified elements or compounds react or partially react to reach a chemical equilibrium state.[35]

Ternary phase diagrams for H, C and O were calculated for three pressure values and two temperature values (see Fig. 6) by assuming real gas behaviour. Under the assumption of thermodynamic equilibrium, the points on the ternary diagram at which the production and consumption of solid graphitic carbon are balanced result in a line that separates the carbon deposition region (carbon activity coefficient = 1) from the no carbon deposition region (carbon activity coefficient < 1).[36] In both diagrams, the positions of three relevant $H_2 : CO_2$ gas mixtures of 0.1 : 0.9, 0.5 : 0.5 and 0.9 : 01 ratio are indicated as dots.

No carbon deposition for these gas compositions is predicted by thermodynamics calculations even at 10 bar and 700 °C. It can be seen that the overall carbon deposition area increases with increasing pressure and decreasing temperature. In the upper triangle delimited by C = 0.25, H = 0.75, and H = 1, however, the probability of carbon formation diminishes with increasing pressure. It is worth mentioning that the present study is restricted to graphitic carbon. When all carbon allotropes are included (not possible in our FactSage version), the carbon deposition region expands, as shown by Jaworski *et al.*[37]

2.3.2 Catalyst exposure tests in a pressurized Ni–Cr tube reactor. Because electrolysis plants are supposed to function at elevated pressures of up to 30 bar for economic reasons, the probability of carburisation increases, as shown in Fig. 6, due to a shift of the Boudouard equilibrium reaction to the solid product side. Therefore, the influence of feed pressure on the activity of the LSCrM, Ni_3Sn_2, GDC_{20} and Ni powder materials for carbon formation was experimentally investigated in a tubular Ni–Cr reactor.

2.3.3 Exposure tests of the catalysts under carbon-rich gas (70% H_2, 10% CO, 10% CH_4 and 10% CO_2) atmosphere for

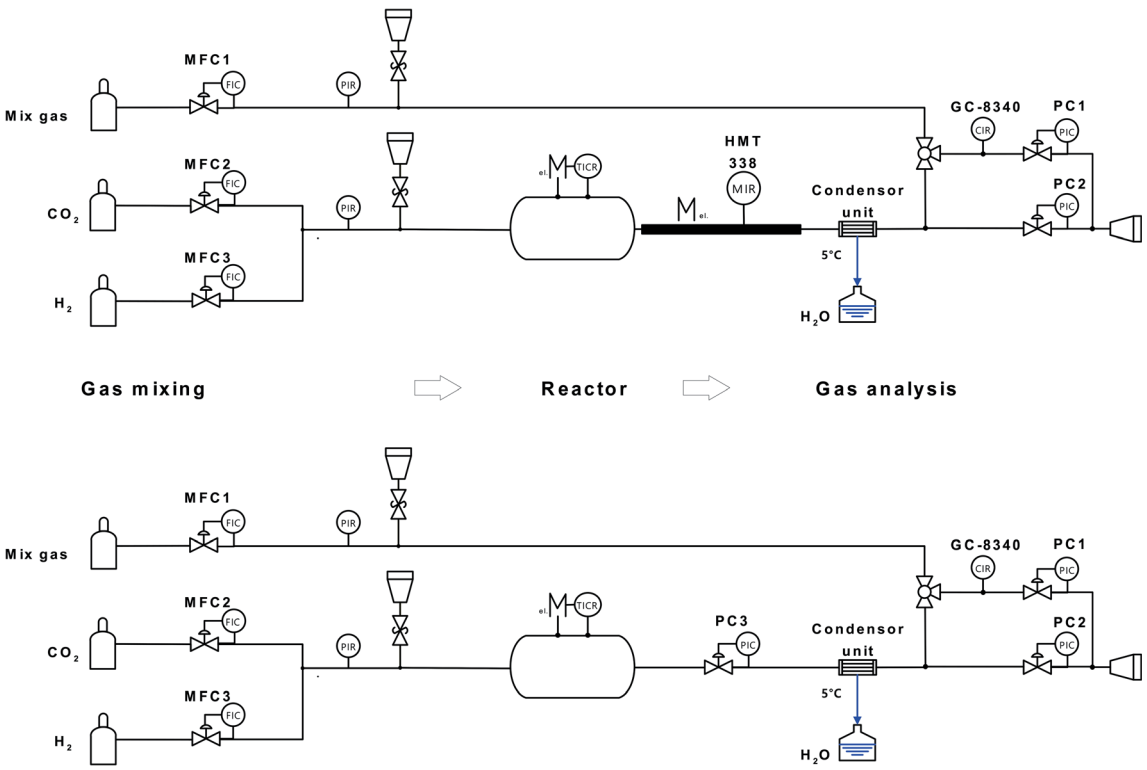

Fig. 9 Scheme of (top) the reactor setup for testing the catalytic activity for the RWGS in a quartz glass tube at ambient pressure and (bottom) exposure test in a metallic tube at pressures up to 10 bar.

100 h at 700 °C and 3 bar. After the first exposure test under the carbon-rich gas mixture, a 23% increase in Ni mass was measured, while no significant changes in the weights of the other samples were observed (see Table S3 in the ESI†). The presence of graphitic carbon in the Ni sample was confirmed by the emergence of an additional XRD reflex at $2\theta = 26.4°$, Raman peaks at 1582 cm^{-1} and 1348 cm^{-1} and black domains in the BSE micrographs (see Fig. 7). No traces of graphitic or amorphous carbon were detected at LSCrM, Ni_3Sn_2 or GDC_{20} after the stability tests.

2.3.4 Exposure tests of the catalyst powder under different $H_2 : CO_2$ atmospheres and temperatures at 10 bar. The choice of the three experimental conditions of (i) 0.9 : 0.1 $H_2 : CO_2$ at 800 °C, (ii) 0.5 : 0.5 $H_2 : CO_2$ at 700 °C, and (iii) 0.1 : 0.9 $H_2 : CO_2$ at 700 °C was motivated by their proximity to the carbon deposition boundary materialized by the green lines for 10 bar in Fig. 6. No significant change in the mass of the LSCrM, Ni_3Sn_2, GDC_{20} or Ni samples was assessed after the 300 h test period. The exposure conditions led to slight changes in the catalyst composition, as listed in Table 3. In terms of particle morphology, however, Ni_3Sn_2 and especially Ni particles were affected by sintering effects, notably after the tests at 800 °C.

The XRD spectra of all the investigated samples revealed no modification of the crystallite structure or indication of carbon formation. The latter was confirmed by Raman analysis of LSCrM, GDC_{20} and Ni. Surprisingly, the d-band peaks at 1610 cm^{-1} and 1342 cm^{-1} corresponding to amorphous carbon were detected at the surface of Ni_3Sn_2 after the exposure tests under 0.5 : 0.5 and 0.1 : 0.9$H_2 : CO_2$ atmospheres at 700 °C.

This type of carbon is not detectable in XRD; therefore, the Ni_3Sn_2 pattern did not show any diffraction peak at $2\theta = 26.4°$. No carbon was visible in the SEM micrographs as well. Fig. 8 shows the Raman spectra of Ni_3Sn_2 and the other samples for comparison after the exposure tests.

3. Conclusions

The catalytic activities of $La_{0.75}Sr_{0.25}Cr_{0.5}Mn_{0.5}O_3$, Ni_3Sn_2 and GDC_{20} powder materials for the RWGS reaction were evaluated in a quartz tube reactor at 700 °C and 800 °C and were compared to that of a commercial Ni powder which is a commonly used catalyst in H_2O/CO_2 HT co-electrolysis cells. Especially, the CO yields at LSCrM and GDC_{20} in a 0.5 : 0.5 $H_2 : CO_2$ ratio at 800 °C were close to thermodynamic equilibrium; therefore, these materials are as active as nickel for RWGS. Moreover, in feeds with high H_2 partial pressure, the samples all exhibited higher selectivity for CO and H_2O products than pure Ni, which catalysed CH_4 by-product formation. To our knowledge, the catalytic activities of the intermetallic Ni_3Sn_2 phase, LSCrM perovskite oxide and GDC_{20} oxide for the reverse water gas shift reaction were demonstrated for the first time in this work.

No carbon formation was observed at these catalysts after 100 h exposure time in a carbon-rich atmosphere at 3 bar and 700 °C in the metallic tube reactor. In contrast, large carbon deposits were detected on Ni under the same conditions. Curiously, after 300 h exposure time in 0.5 : 0.5 and 0.1 : 0.9 $H_2 : CO_2$ atmospheres at 10 bar and 700 °C, traces of amorphous carbon were detected by Raman spectroscopy only on the Ni_3Sn_2 surface. After both catalytic and exposure experiments, XRD and SEM analysis revealed excellent redox behaviour and stable morphologies of LSCrM and GDC_{20}, slight phase segregation of Ni_3Sn_2 into NiO and SnO_2 and, finally, strong sintering activity of Ni and of Ni_3Sn_2 powder to a lesser extent.

4. Experimental

$La_{0.75}Sr_{0.25}Cr_{0.5}Mn_{0.5}O_{3-\delta}$ was synthesized by a sol–gel route. Citric acid ($C_6H_8O_7 \cdot H_2O$, Sigma-Aldrich) and EDTA ($C_{10}H_{16}N_2O_8$, Sigma-Aldrich) were dissolved in ultrapure water (PURELAB® Ultra, Elga LabWater). Under continuous stirring, stoichiometric amounts of lanthanum nitrate ($La(NO_3)_3 \cdot 6H_2O$, 14.3 g, 33.0 mmol, 0.75 eq.), strontium nitrate ($Sr(NO_3)_2$, 2.36 g, 11.2 mmol, 0.25 eq.), chromium nitrate ($Cr(NO_3)_3 \cdot 9H_2O$, 8.84 g, 22.1 mmol, 0.50 eq.) and manganese nitrate ($Mn(NO_3)_2$, 4.25 g, 23.8 mmol, 0.50 eq.) (99.99%, all AlfaAesar) were dissolved in this solution. The pH of the mixture was adjusted to 7 by addition of ammonium hydroxide solution. Subsequent evaporation of excess water at mild temperatures ($\approx$150 °C) resulted in a homogeneous gel, which was fired at 350 °C for 3 h. The resulting powder was coarsely ground in a mortar and treated at 600 °C for 2 h in ambient air. Finally, the calcination step was performed in synthetic air (99.995%, basi Schöberl) at 1100 °C for 16 h.

Ni_3Sn_2 was prepared in a centrifugal casting induction oven by melting stoichiometric amounts of Ni and Sn (42.6 g, 3 eq. Ni and 57.4 g, 2 eq. Sn, 99.9%, MaTecK) for 5 min under vacuum. After cooling, the ingot was mechanically crushed and ball-milled (Retsch PM100) twice for 8 h using zirconium oxide balls.

Commercial GDC_{20} (99.9%, Kerafol) and Ni (99.9%, Vale Inco.) were used as received.

The crystallographic structures of the materials were examined by X-ray diffraction analysis (D8 Advance, Cu-K_α, Bruker). To increase the surface sensitivity, a Goebel mirror was used for the solid samples. The surface morphology of the materials was analysed by scanning electron microscopy (SEM) and energy dispersive X-ray spectroscopy (EDX) (XL40, EDAX CDU Leap detector, Phillips). Carbon formation was evaluated by a confocal microprobe Raman spectrometer (InVia Reglex, Renishaw). The laser beam (Ar, 532 nm, 1 mW) was focused through a 50× objective lens (DM 2500, Leica) with ~1 μm spot size. The spectral range and resolution were 100 to 3200 cm^{-1} and 1 cm^{-1} at room temperature, respectively. BET surface area measurements were performed with an Autosorb IQ3 station (Quantachrome).

A schematic of the experimental setup for evaluation of the catalyst activity for RWGS is shown in Fig. 9. The hydrogen (5.0, Soboth)/carbon dioxide (4.5, Soboth) gas inlet composition ($x(H_2)$ and $x(CO_2)$) was controlled by two mass-flow controllers (5850, Brooks). The total flow rate was kept constant at 100 ml min^{-1}. The reactor consisted of a quartz glass tube ($\varnothing$ = 5 cm, $L_{hot\text{-}zone}$ = 30 cm, $V_{hot\text{-}zone}$ = 590 cm^3) positioned in a 3-zone horizontal furnace (hot-zone 300 mm length) with a theoretical residence time in the hot-zones of 1.46 min (gas velocity 358 ml min^{-1}) and 1.33 min (392 ml min^{-1}) at 700 °C and 800 °C, respectively. To avoid heat loss, the inlet and outlet

zones of the reactor tube inside the oven were sealed by porous Al_2O_3/SiO_2 stoppers (Promatron®-23 HD) with 9 mm holes. Due to thermal expansion of the gas at the inlet of the isothermal zone, the gas velocity increased inside the reactor. Powder samples were placed in an aluminium oxide crucible (volume ratio of reactor hot-zone to aluminium oxide crucible ≈ 15 : 1) in the middle of the glass tube (non-fixed-bed reactor).

Due to the different bulk material densities, the hourly space velocities in the range of 1000 h^{-1} for LSCrM and 2000 h^{-1} for the Ni powder catalyst with a bed volume of 1,5–3 ml were calculated. The reactor outlet tubing and the humidity sensor (HMT 330, Vaisala) were heated to 120 °C to prevent condensation. Before analysis by gas chromatography (GC), water was separated from the gas phase by passing through a reflux condenser at 5 °C. At the condenser outlet, gaseous reaction educts and residual products were detected by a gas chromatograph (GC8340, Fisons) equipped with two separation columns: one with a methanizer with a flame ionization detector and one with a thermal conductivity detector. The GC sample loop flow was controlled by the pressure difference between the two pressure controllers (5800E, Brooks), and the overpressure was maintained at 25 mbar. GC calibration was performed daily with a gas mixture of defined composition (Air Liquide).

For exposure tests at 3 and 10 bar, the quartz glass reactor was replaced by an ET45 Ni–Cr alloy tube (3.8 cm inner diameter, 340 cm^3 hot-zone volume, 58 and 52 s residence times at 700 °C and 800 °C, respectively). The humidity sensor was disassembled from the reactor and a back-pressure controller (5866, Brooks) was connected to the reactor outlet to maintain the desired pressure inside the reactor.

All tests were performed with a non-fixed-bed reactor because not only the catalytic activity of the powder materials but also their affinity for sintering was of practical interest. For the catalytic tests in different $H_2 : CO_2$ atmospheres at 1 bar, 4 g of the powder material was placed in a ceramic crucible in the reactor and heated to the desired temperature (3 K min^{-1}) of 700 °C or 800 °C in 10% H_2/Ar reducing atmosphere before pure H_2, $H_2 : CO_2$ gas mixtures with different compositions and finally pure CO_2 were introduced into the reactor. Gas chromatograms were recorded after a 2 h waiting time at a defined set point. Exposure tests were performed in a similar way.

After heating the samples to the desired temperature, the pressure was increased and the exposure tests were performed for 300 h at three different $x(H_2)$ and $x(CO_2)$ inlet molar fractions and two different temperatures:

(i) $x(H_2) = 0.9$, $x(CO_2) = 0.1$ @ 800 °C.
(ii) $x(H_2) = x(CO_2) = 0.5$ @ 700 °C.
(iii) $x(H_2) = 0.1$, $x(CO_2) = 0.9$ @ 700 °C.

The exposure test @ 700 °C was performed at 3 bar for 100 h in a special carburisation-active mixture of $x(H_2) = 0.7$, $x(CO_2) = 0.1$, $x(CO) = 0.1$ and $x(CH_4) = 0.1$. After the tests, all samples were cooled in a reducing 10% H_2/Ar atmosphere at 1 bar.

Conflicts of interest

There are no conflicts to declare.

Acknowledgements

The authors gratefully acknowledge funding by the German Federal Ministry of Education and Research (BMBF) within the Kopernikus Project P2X (03SFK2U0) : Flexible use of renewable resources – exploration, validation and implementation of 'Power-to-X' concepts as well as all project partners for fruitful cooperation and discussions.

Notes and references

1 Q. Fu, C. Mabilat, M. Zahid, A. Brisse and L. Gautier, *Energy Environ. Sci.*, 2010, **3**, 1382.
2 Y. Wang, T. Liu, L. Lei and F. Chen, *Fuel Process. Technol.*, 2017, **161**, 248.
3 X. Zhang, Y. Song, G. Wang and X. Bao, *J. Energy Chem.*, 2017, **26**, 839.
4 C. Stoots, J. O'Brien and J. Hartvigsen, *Int. J. Hydrog. Energy*, 2009, **34**, 4208.
5 S. Diethelm, J. V. Herle, D. Montinaro and O. Bucheli, *Fuel Cells*, 2013, **13**, 631.
6 S. W. Kim, H. Kim, K. J. Yoon, J. H. Lee, B. K. Kim, W. Choi, J. H. Lee and J. Hong, *J. Power Sources*, 2015, **280**, 630.
7 Y. Tao, S. D. Ebbesen and M. B. Mogensen, *J. Power Sources*, 2016, **328**, 452.
8 X. Yang and J. T. S. Irvine, *J. Math. Chem.*, 2008, **18**, 2349.
9 S. D. Ebbesen and M. Mogensen, *J. Power Sources*, 2009, **193**, 349.
10 T. Chen, W. G. Wang, H. Miao, T. Li and C. Xu, *J. Power Sources*, 2011, **196**, 2461.
11 J. Zhang and D. J. Young, *Corros. Sci.*, 2007, **49**, 1496.
12 Y. Tao, S. D. Ebbesen, W. Zhang and M. B. Mogensen, *ChemCatChem*, 2014, **6**, 1220.
13 W. Wang, C. Su, Y. Wu, R. Ran and Z. Shao, *Chem. Rev.*, 2013, **113**, 8104.
14 N. Bogolowski, B. Iwanschitz and J.-F. Drillet, *Fuel Cells*, 2015, **15**, 711.
15 U. Guharoy, E. Le Saché, Q. Cai, T. R. Reina and S. Gu, *J. CO_2 Util.*, 2018, **27**, 1.
16 D. Maiti, Y. A. Daza, M. M. Yung, J. N. Kuhn and V. R. Bhethanabotla, *J. Mater. Chem. A*, 2016, **4**, 5137.
17 S. E. Yoon, J. Y. Ahn, B. K. Kim and J. S. Park, *Int. J. Hydrogen Energy*, 2015, **40**, 13558.
18 X. Yue and J. T. S. Irvine, *J. Mat. Chem. A*, 2017, **5**, 7081.
19 M. Torrell, S. Garcia-Rodriguez, A. Morata, G. Penelas and A. Tarancon, *Faraday Discuss.*, 2015, **182**, 241.
20 F. Bustamante, R. M. Enick, A. V. Cugini, R. P. Killmeyer, B. H. Howard, K. S. Rothenberger, M. V. Ciocco, B. D. Morreale, S. Chattopadhyay and S. Shi, *AIChE J.*, 2004, **50**, 1028.
21 G. Pekridis, K. Kalimeri, N. Kaklidis, E. Vakouftsi, E. F. Iliopoulou, C. Athanasiou and G. E. Marnellos, *Catal. Today*, 2007, **127**, 337.
22 Q. Sun, C. W. Liu, W. Pan, Q. M. Zhu and J. F. Deng, *Appl. Catal., A*, 1998, **171**, 301.
23 S. I. Fujita, M. Usui and N. Takezawa, *J. Catal.*, 1992, **134**, 2.

24 S. S. Kim, H. H. Lee and S. C. Hong, *Appl. Catal., A*, 2012, **423–424**, 100.
25 K. Zhao, Q. Bkour, X. Hou, S. W. Kang, J. C. Park, M. G. Norton, J. I. Yang and S. Ha, *Chem. Eng. J.*, 2018, **336**, 20.
26 L. Wang, H. Liu, Y. Liu, Y. Chen and S. Yang, *J. Rare Earths*, 2013, **31**, 969.
27 S. Choi, B.-I. Sang, J. Hong, K. J. Yoon, J.-W. Son, J.-H. Lee, B.-K. Kim and H. Kim, *Sci. Rep.*, 2011, **7**, 41207.
28 A. Wolf, A. Jess and C. Kern, *Chem. Eng. Technol.*, 2016, **39**, 1040.
29 M. Mogensen, T. Lindegaard, U. R. Hansen and G. Mogensen, *J. Electrochem. Soc.*, 1994, **141**, 2122.
30 M. Mogensen, N. M. Sammes and G. A. Tompsett, *Solid State Ionics*, 2000, **129**, 63.
31 H. Liu, C. Zhao and L. Wang, *J. Chem. Eng. Jpn.*, 2016, **49**, 16.
32 M. Kovacevic, B. Mojet, J. van Ommen and L. Lefferts, *Catal. Lett.*, 2016, **146**, 770.
33 Y. A. Daza, R. A. Kent, M. M. Yung and J. N. Kuhn, *Ind. Eng. Chem. Res.*, 2014, **53**, 5828.
34 P. Tanasini, M. Cannarozzo, P. Costamagna, A. Faes, J. Van Herle, A. Hessler-Wyser and C. Comninellis, *Fuel cells*, 2009, **5**, 740.
35 C. W. Bale, P. Chartrand, S. A. Degterov, G. Eriksson, K. Hack, R. Ben Mahfoud, J. Melancon, A. D. Pelton and S. Petersen, *Calphad*, 2002, **26**, 189.
36 H. Sartipizadeh, T. L. Vincent and R. J. Kee, *Proceedings of the American Control Conference, ACC 2015*, Chicago, IL, USA, July 1-3, 2015, p. 5641.
37 Z. Jaworski, B. Zakrzewska and P. Pianko-Oprych, *Rev. Chem. Eng.*, 2016, **33**, 217.

